EUROPEAN ORGANISATION FOR NUCLEAR RESEARCH

CERN–PPE/91–130
August 21, 1991

Particle Identification with the OPAL Jet Chamber

M. Hauschild, R.-D. Heuer, C. Kleinwort[a]
CERN, Geneva, Switzerland

J. Ludwig, W. Mohr, D. Schaile, O. Schaile, C. Wahl
Fakultät für Physik, Universität Freiburg, Freiburg, FRG

P. Bock, A. Dieckmann, P. Igo-Kemenes, P. Lennert, H. von der Schmitt, A. Wagner
Physikalisches Institut, Universität Heidelberg, Heidelberg, FRG

[a]Now at II. Inst. für Experimentalphysik, Universität Hamburg, FRG

Abstract

The jet chamber of the OPAL experiment at the e^+e^--collider LEP is designed to measure the momentum of charged particles as well as the specific energy loss in the chamber gas. In this paper, the calibration procedure for the energy loss measurement is described in detail. A resolution of (3-4)% has been achieved allowing identification of particles with momenta up to 20 GeV/c in dense particle environments typical for events from Z^0 decays.

(submitted to Nucl. Instr. and Meth.)

1 Introduction

In the analysis of e^+e^- collisions, particle identification capabilities provide access to a wide range of physics topics, one example being heavy quark identification using lepton tags. Hadronic decays of the Z^0 boson - produced copiously at LEP - result in a mean multiplicity of about 20 charged particles, most of them in rather dense particle jets. The main tool used in the OPAL experiment [1] at LEP for the identification of charged particles is a large drift chamber ("jet chamber") [2, 3]. It combines good space and double track resolution over a solid angle close to 4π with the possibility of particle identification through the measurement of the energy loss in the chamber gas.

The energy loss dE/dx of particles in matter is described by the Bethe-Bloch equation [4]. It is a universal function of $\beta\gamma$ for all particle masses. The energy loss as function of momentum shows a characteristic decrease with $1/\beta^2$, reaches a minimum around $\beta\gamma = 4$, and continues with a logarithmic rise ("relativistic rise region") until it saturates ("Fermi plateau"). By measuring the momentum of a particle as well as its energy loss, the mass of the particle can be determined. This method of particle identification has been used in recent years by several experiments [5, 6, 7, 8, 9]. Detailed models have been developed which allow the calculation of particle energy losses for many gases [10]. Typical curves are shown in fig. 1, where the energy loss is plotted as a function of the particle momentum.

Due to the small difference in energy loss between the particle species (e.g. at 10 GeV/c the difference in mean dE/dx between pions and electrons is about 10%), the application of an energy loss measurement for the identification of relativistic particles faces several constraints. The energy loss distribution (approximately a Landau-distribution) has a large inherent width of 60 to 70% (FWHM for a path length of 1 cm of gas at atmospheric pressure). This makes it necessary to measure many samples along each track in order to determine the mean energy loss with sufficient accuracy. Reduction of the fluctuations of the energy loss can also be achieved by using thicker samples, for example by increasing the gas pressure. However, increasing the thickness results in a lower Fermi plateau (see e.g. [11]) and a different slope of the relativistic rise and therefore smaller differences in the energy loss of different particle species. The figure of merit which has to be optimised is not the resolution but the particle separation power expressed as resolution normalised to the energy loss difference. For commonly used drift chamber gases, the optimum value for the separation power is at a pressure of 3 to 4 bar [11, 12]. An extensive study of the separation power in this pressure range has been performed with a full scale prototype (FSP) [13] of the OPAL drift chamber. Systematic errors must be kept below a level of 1–2%. Corrections which depend on track direction and background conditions must therefore be known to this precision.

In this paper, a brief description of the jet chamber is first given. The procedure to determine and calibrate the specific energy loss of a particle is then described in detail in chapter 3. The corrections applied to the data and the resolutions achieved are also presented there. The parametrisation used to describe the measured energy loss curves is shown in chapter 4 where in addition the particle separation power is presented.

2 Jet Chamber

The central tracking system of the OPAL detector [1] at the e^+e^-storage ring LEP consists of three elements: a high resolution vertex chamber close to the interaction point, a large pictorial drift chamber of the "jet chamber" type as the main tracking detector and a set of outer drift chambers ("z-chambers") for a precise measurement of the z-coordinate of each track along the beam direction. The jet chamber

is designed to measure space points of tracks and the energy loss of particles by multiple sampling of the ionisation along a track. It is operated in a magnetic field of 0.435 T. Over a solid angle of 73% of 4π, 159 points are measured along each track. With at least 8 points on a track a solid angle of 98% of 4π is covered. At each point true three–dimensional coordinates are determined from the wire position (r), the drift time (ϕ) and from a charge division measurement (z). The ratio of the integrated charges for each hit at both wire ends determines z,and the sum is used to calculate the energy loss, dE/dx. The main features of the jet chamber are described in the following sections, and more details may be found in [2], [3] and [14].

Mechanical design

The sensitive volume of the jet chamber is a cylinder with a length of about 4 m, surrounding the beam pipe and the vertex chamber. The chamber is subdivided into 24 identical sectors, each containing a sense wire plane with 159 sense wires and two cathode wire planes which form the boundaries between adjacent sectors.

A schematic drawing of the jet chamber is shown in fig. 2. The sense wires, equally spaced by 10 mm and alternating with potential wires, are located between radii of 255 mm and 1835 mm. The maximum drift distance varies between 3 cm at the innermost sense wire and 25 cm at the outermost wire. In order to resolve the left-right ambiguities, the sense wires are staggered by ± 100 μm alternately to the left and right side of the plane defined by the potential wires. The sense wires are at ground potential. The voltage at the potential wires determines the gas gain and is normally maintained at -2.38 kV.

The wires are stretched between two conical end plates which are held apart by a shell of 24 hollow aluminum panels located at the outer radius of the cylinder. There is no inner support tube. The wires run through slots between field shaping electrodes, situated on the inside of the conical endplates, and then through holes in those plates to the outside.

High voltage system

The high voltage system has to supply voltages ranging from -25 kV at the outer feed points to -2.5 kV at the inner feed points of the cathodes. In order to avoid non-linearities in the drift field, caused for example by leakage currents and by the presence of large ion currents under certain beam conditions, four intermediate points are also supplied with high voltage. All 24 cathode planes are connected to the same power supplies to guarantee the same voltages throughout the chamber. The currents flowing into the resistor chains of the cathodes are monitored separately at each feed point of each cathode with high accuracy; for example, the current of 600 μA per cathode drawn at the outer feed point is measured with a resolution of 8 nA.

Under normal operating conditions, all potential wires are connected to one power supply. The currents in the chamber are monitored for each group of 16 wires using current meters similar to those used for the cathodes, but with a resolution of 1 nA. The sense wire currents are monitored with a precision of 8 nA, again in groups of 16 wires. More details about the high voltage system can be found in [3] and [15].

Gas system

The chamber is operated with a three-component gas mixture of 88.2% argon, 9.8% methane and 2.0% isobutane at a pressure of 4 bar. The gas system was built as a closed system with recirculation and purification of the gas in order to keep gas properties such as drift velocity and electron attachment stable over a period of several months in the presence of outgassing materials. Oxygen, which has a large attachment coefficient, can be eliminated with high efficiency down to a level of a few ppm: with one volume exchange per day the oxygen level reaches values as low as 2 ppm after a few days

of purification.

To control the gas quality, two monitoring systems are used. Inside the pressure vessel of the jet chamber, 20 proportional tubes equipped with ^{55}Fe sources measure the gas gain and 64 thermistors the gas temperature. Together with the pressure measurement this allows monitoring of the density. In addition a special external drift chamber is used to monitor drift velocity and electron attachment. This chamber is described in detail in [16].

Readout electronics
Low-noise preamplifiers are mounted onto the end plates close to the points where the sense wires are attached. The waveforms of the amplified signals from each end of every sense wire are recorded with 100 MHz flash analogue-to-digital converters (FADCs). The components of the FADC system (DL300) are described in detail elsewhere [17]. The FADCs have a 6-bit resolution, which is effectively extended to 8-bits by a nonlinear response function. The digitised data are stored in fast memories which are 256 (or 1024) samples deep. After a valid trigger has occured, this information is read out via hardware scanners, which also perform zero suppression. The calculation of drift times, charges and z-values is performed online in a microprocessor system. All pulses are linearised according to the transformation $A_l = A_{nl}/(1-\alpha A_{nl}/64)$, where A_l and A_{nl} are the linearised and nonlinear FADC values, respectively. The factor α (α=0.75) describes the feedback in the electronics used to obtain the nonlinear response. After linearisation, a pedestal is subtracted bin by bin. Hits are recognised using a "difference of samples" algorithm [18]. At the least, there must be a recognizable rising edge at one end of a wire, i.e. the difference between 2 differentiated linearised bin contents has to be $\geq$1.2, and the integral of the rising part of the pulse has to be $\geq$12 counts. The charge of a pulse is obtained by integrating each pulse over 200 ns with respect to the start of the pulse.

Working point
The choice of the working point of the chamber faces different conflicting requirements. Long drift distances (up to 25 cm in this case) require high gas pressure to minimise diffusion effects which deteriorate the spatial resolution. Good momentum resolution for low momentum particles requires low density to reduce multiple scattering. The chosen gas pressure of 4 bar is a compromise between these requirements which at the same time optimises the particle separation power [13].

The charge division method for the determination of the z-coordinate along the wire requires high gas gain in order to achieve a high signal to noise ratio. On the other hand, the energy loss measurement requires low gas gain to minimise corrections due to saturation effects as discussed later. The chosen gas gain of approximately 10^4 is again a compromise between these conflicting requirements.

The chamber is operated at a drift field of 890 V/cm where the drift velocity is approximately saturated at a value of 52.7 μm/ns. The Lorentz angle by which the driftpaths are tilted due to the magnetic field is measured to be α_L=20.0°.

The resolutions obtained with the chosen working point are as follows: $\sigma_\phi = 130$ μm, averaged over the entire drift space, resulting in a momentum resolution of $\sigma_{p_t}/p_t = \sqrt{0.02^2 + (1.5 \cdot 10^{-3} \cdot p_t)^2}$ (p_t in GeV/c), where the first term represents the contribution from multiple scattering. Two neighbouring hits are resolved with a probability of greater than 95% at distances greater than 4 mm between successive hits. The single hit resolution in z is $\sigma_z = 6$ cm, with remaining systematic contributions due to induction currents.

Stability requirements for energy loss measurements
Particle identification by measurement of the energy loss in the region of the relativistic rise puts high demands on the stability of the energy loss measurement (~1%) and therefore on the stability

of several detector parameters. In the following the requirements necessary to reach this stability are discussed.

- Gas density.
  To achieve a stability of the gas gain of $\Delta G/G = 1\%$, the gas density ρ has to be kept constant within $\Delta\rho/\rho \approx 0.2\%$. To reach this value in a closed gas system, time dependent temperature gradients must be kept below 0.6° C. The measured variation during data taking was ΔT<0.1° C during a period of one week. More problematic was the effect of several small leaks (~40 ℓ_{ntp}/hour compared to the total volume of 200,000 ℓ_{ntp}) leading to a decrease in pressure which was approximately compensated by adding gas. The necessary corrections will be discussed later.

- High voltage.
  The gas gain depends on the surface field of the sense wire E_a, which is determined by the voltage applied to the potential wires U_p and by the drift field E_d. Field calculations [19] and measurements [13] yield the conditions $\Delta E_d \leq 1.2$ V/cm at the operating point of E_d=890 V/cm and $\Delta U_p \leq 1.4$ V for U_p= 2380 V that are met by the power supplies used [20]. Changes of the cathode current during the operation of the chamber were measured to be smaller than 300 nA, corresponding to ΔE_d<0.3 V/cm. The dark current of each group of 16 potential wires was less than 1 nA, the currents during data taking were on the order of 5 nA, and the voltage fluctuations were measured to be below 0.1 V.

- FADC pedestals.
  The pedestals in the FADCs have to be monitored to high accuracy. For the mean integrated charge of 250 counts obtained for a minimum ionising particle summed over both wire ends and using an integation length of 200 ns (corresponding to 20 FADC samples), the pedestals must be known to an accuracy of about 0.1 counts or 1%. The pedestal values showed a stability of better than 0.03 counts for any channel over a period of one week.

- Electronics gain.
  The knowledge of the relative electronics gain for the two readout channels of each wire is important for the charge measurement. This gain ratio is calibrated and monitored using a laser system installed for general monitoring purposes [21], and was stable to within 1% over a period of several months. The absolute electronics gain for the individual wires is taken into account together with the gas gain calibration.

3 Determination of the energy loss

Before the mean energy loss of a track can be calculated, the raw charges determined online are subject to quality cuts and corrections. In this chapter all quality cuts and corrections are described and the achieved resolutions are presented.

3.1 Quality cuts

- Only hits assigned to the track in the final fit in the $R\phi$–plane are used for the determination of the truncated mean.

- Due to the jet-like structure of the multihadronic events in e^+e^- collisions, hits with a small separation are rather frequent. For a hit to be accepted in the calculation of the truncated mean, the following criteria should be met:
  - No second hit should be present within the integration length of ± 200 ns.
  - If parts of tracks are closer than the double hit resolution of $\sim$3 mm, the individual hits are no longer resolved and only a single hit is found. These hits are discarded.
- Hits should have a minimum distance to the sense wire plane of at least 2 mm.
- For tracks crossing a sector boundary the last (or first) hit within the sector is discarded if it is closer than 1 cm to the boundary.

For isolated tracks, $\sim$7.5% of the hits per track, and $\sim$35% of the hits for tracks in multihadronic events are lost on average by these requirements.

3.2 Corrections

The corrections have been derived from muons in events of the type $e^+e^- \to \mu^+\mu^-$ and from minimum ionising pions (p=(400–800) MeV/c) selected within multihadronic events. Many of the corrections (such as saturation, attachment, and cross talk) depend on each other and were therefore derived iteratively. All corrections are applied on the individual hits rather than on tracks, although for corrections that depend on the track direction, pattern recognition information is needed.

Electronics corrections
If a recorded pulse is shorter than the nominal integration time of 200 ns, the charge is corrected according to a reference pulse shape which has been obtained by averaging a large sample of measured pulses. All measured charges are corrected for the different electronics gain factors at both wire ends which have been determined using the laser system mentioned above. About 0.6% of all hits have at least one bin of the FADC pulse in the overflow (corresponding to an energy loss of approximately 20 times the loss of a minimum ionising particle at normal incidence with respect to the wire). These hits are corrected for the overflow. It has been found that the preamplifiers show a distinct nonlinearity resulting in an underestimate of small charges. Within the range of charges measured, this effect could be neglected.

The amplitudes at both wire ends are then summed and are subjected to the corrections described below.

Multiple hits
Charges of subsequent hits have to be corrected for the tail of all preceeding pulses up to a distance of 4 cm, by using the same reference pulse shape as mentioned above (see fig. 3).

Saturation
At a gas gain of approximately 10^4 used to operate the jet chamber, saturation effects can be observed. The magnitude of the saturation depends on the density of the electrons in the avalanche developing near the wire. This can be explained by a screening of the electric field near the sense wire due to the remaining ions from the amplification of the first arriving electrons. Therefore, the largest effect is observed for tracks running perpendicular to the wires (θ=90°) where the electrons reach the wire almost all at the same spot, and for short drift times where the electron cloud is not spread out by

diffusion in the gas. On the other hand, the saturation gets small for large drift times and for inclined tracks. Since this correction depends on the primary ionisation, it has to be applied to the measured charges Q_{meas} before any other correction is done. Figure 4 shows the dependence of the saturation on the track inclination and the measured charge. The drift time dependence has been found to be negligible in this experiment, and the following correction function is used:

$$Q_{corr} = Q_{meas} \cdot \frac{1+a}{1+a \cdot |cos\theta|} ,$$

where the free parameter a depends on the measured charge $\{a = a(Q_{meas})\}$ and is determined from the data. Its value is different for different regions of the energy loss curve:

$$\begin{array}{ll} a = 0 & \text{for } Q_{meas} \leq Q_{min} \\ a = (Q_{meas} - Q_{min}) \cdot s & \text{for } Q_{min} < Q_{meas} < Q_{max} \\ a = 0.2 & \text{for } Q_{meas} \geq Q_{max} \end{array}$$

where the parameter values were determined as follows:

$$Q_{min} = 3.291 \text{ keV} \quad Q_{max} = 10.915 \text{ keV} \quad \text{and } s = 0.02623 \text{ (keV)}^{-1} .$$

As a result of the saturation correction, the energy loss dependence on the track angle θ essentially disappears.

Track length

The measured charges Q_{meas} are in first approximation proportional to the track length and therefore have to be normalised to 1 cm sample thickness according to the determined flight direction. This normalisation depends on the angle θ of the track with respect to the wire or beam direction and on the angle δ relative to the drift direction taking into account the Lorentz angle of 20.0°: $Q_{norm} = Q_{meas}/(\sin\theta \cdot \sin\delta)$. An additional logarithmic length dependence of the energy loss expected theoretically (see chapter 4 for details) is not corrected for. Its small contribution has been absorbed in other corrections.

Staggering

Because of the wire staggering (± 100 μm mechanical and 57 μm maximum electrostatic), a slightly different width of the driftspace for wires on the same and on the opposite side of the wire plane with respect to the track position is observed. The resulting difference of 10% in the collected charge is corrected for, neglecting the small z dependence due to the electrostatic bowing.

Cross Talk

During signal formation at a sense wire, small signals of opposite polarity are induced on adjacent wires. Detailed calculations of the signal propagation [22] provided the values for the electrical termination of all wires to equalise the shape of the pulses for the direct and cross talk signals. This allowed the addition of a passive resistor network at the output of the preamplifiers to compensate the effect of the cross talk for the next two neighbouring wires. Since the compensation is not complete, a small dependence of the charge on the track angle ϕ with respect to the sense wire plane (ϕ_{local}) is observed as shown in fig. 5. A polynomial function is fitted to the data (solid line in fig. 5) and used as a correction. The residual cross talk was measured to be ~6%, in good agreement with field calculations.

Curvature dependent effects

The mean inclination of a track with respect to the drift direction gets larger with increasing curvature causing a change in the arrival time distribution of the drifting electrons at the wire, and therefore a change in the recorded pulse shape. The tilt of the drift paths due to the magnetic field results in a

difference of the truncated mean values for negative and positive particles with the same momentum. The effect is small in this experiment (see fig. 5 at large angles ϕ_{local}) and has been absorbed in the correction for the cross talk described above.

Attachment
Due to small electronegative contaminations present in the gas, a fraction of the electrons produced by the primary ionisation process is lost during the drift to the anode. Measurements performed with the monitoring chamber showed a signal reduction of approximately 2% for an oxygen content of 2 ppm for a drift distance of 20 cm compared to signals from short distances. The average drift distance in the chamber is 7 cm resulting in an average signal loss of only 0.7%. Therefore, no correction has been applied for this effect.

Gas Gain
For each wire the amplification factors can be slightly different due to small differences in the electric field or in the gain constants of the amplifiers. In addition, systematic differences at the sector boundaries (see fig. 6) due to electric field distortions have to be accounted for. All gain differences are corrected using calibration factors derived from the data.

Density
As already mentioned above, the pressure and therefore the density ρ was not stable due to several small leaks. Due to changes in the leak compensation, the gas density varied during data taking in 1990 by up to 1.9%. The gas gain changed accordingly as indicated in fig. 7, where the measured charge for muons from dimuon events is shown as a function of the gas density. A fit to these data results in

$$\frac{\Delta(dE/dx)}{(dE/dx)} = -5.1 \cdot \frac{\Delta\rho}{\rho} .$$

A typical time scale for readjustments of the density correction was of the order of one week.

Space charge
The stability of the drift field and of the gas gain is limited by the buildup of space charge from positive ions drifting away from the anode to the cathode. The amount of space charge depends on the rate of tracks (essentially from beam induced background) and synchrotron radiation as well as on the gas gain itself. Monitoring of the chamber currents is essential in order to correct for this effect. The effect and its correction has been studied in a test beam with the FSP [13] and in the JADE experiment at PETRA. Since in the test beam measurements all ionisation was produced in a rather small beam spot, the JADE measurements give a more realistic picture of the effects of ionisation produced in the whole chamber. At JADE a change in gain of the order of 0.7% per 100 nA current drawn in a group of 16 sense wires was observed [23]. Since in this experiment the maximum current measured during data taking was 50nA, no correction was needed to be applied.

3.3 Truncated mean

After the quality cuts and corrections described above, N independent energy loss measurements per track are available. The most precise way to extract the information from these measurements is the use of a maximum likelihood method comparing the measured distribution with a Landau distribution. A much simpler procedure, which is almost as accurate, but uses much less computing time, is the method of the truncated mean [24]. This method rejects certain percentages of the lowest and highest of the N measured dE/dx values from the calculation of the mean energy loss. The fraction of hits to be rejected is determined by optimising the resolution. In this experiment the highest 30% of the

charges are truncated and no truncation is performed at the lower tail of the Landau distribution (in contrast to the measurements with the FSP [13]).

The resolution of the energy loss measurement using the method of the truncated mean depends on the number N of samples used. This dependence has been studied using isolated tracks as well as with tracks in dense particle environments. The relative resolution $\sigma(dE/dx)/(dE/dx)$ is plotted in fig. 8 as a function of N, where the data points are obtained by successively (but randomly) increasing the number of samples used for the calculation of the truncated mean per track from 2 to N. A fit to the data yields

$$\frac{\sigma(dE/dx)}{(dE/dx)} \propto N^{-0.43} .$$

A similar result has been obtained for example in [12]. The exponent differs from -0.5 (as expected for a gaussian distribution) since the truncated mean distribution is – for the given number of samples – close to, but not exactly a gaussian distribution. The dependence on N is slightly different for isolated tracks and tracks in a dense particle environment. This is probably caused by an insufficient multiple hit correction resulting in a resolution which is slightly worse than expected.

The measured truncated mean for multihadrons and for dimuons is shown in fig. 9a as a function of momentum for tracks with $N \geq 130$. The theoretical expectations for the different particle species, obtained from a fit to the data as described in the following chapter, are indicated by the solid lines in the figure. Figs. 9(b-e) show the distribution of the truncated mean for tracks in multihadronic events in different momentum slices and for dimuons. The resolutions obtained for $N \geq 130$ are

$$\frac{\sigma(dE/dx)}{(dE/dx)} = 3.1\% \quad \text{for dimuons}$$

and

$$\frac{\sigma(dE/dx)}{(dE/dx)} = 3.8\% \quad \text{for minimum ionising pions in jets.}$$

No dependence of the resolution on the particle momentum has been observed. The fact that the resolution for tracks in dense environments is slightly worse than for isolated tracks can again be attributed to the insufficient multiple hit correction. Extrapolating from the mean number of hits measured to the maximum possible of 159 yields resolutions of 3.0% and 3.8% for dimuons and tracks in jets, respectively. These numbers can be compared with the expectation of 3–4% derived from test beam measurement with the FSP [13]. The resolution obtained with the final chamber during physics data taking compares well with this expectation. The resolution figures given above are an average over the entire run period 1990 which lasted approximately 5 months (corresponding to about 140,000 collected hadronic Z^0 decays). This illustrates the stability of the measurements and the robustness of the calibration already achieved. Also, the resolution achieved during the present data collection compares well with the results from 1990.

4 Parametrisation of the energy loss function

For physics applications, the important measure is the particle separation power rather than the resolution itself. The power to separate particle A from particle B is defined as

$$D = \frac{(dE/dx)_A - (dE/dx)_B}{\sigma(dE/dx)_B} .$$

In order to determine for a particle the most likely mass hypothesis from the measured momentum p and specific energy loss ϵ, the functional dependence of $\epsilon = \epsilon(\beta, \gamma)$ must be known with a precision of better than 1% over the entire momentum range of interest.

In thin absorbers like drift chamber gases, the energy loss occurs due to a small number of collisions causing large fluctuations described by a Landau-distribution with a long tail extending to very large values of energy loss due to δ-electrons that are produced in hard collisions. Calculations of the resulting energy spectrum are not valid for the case of drift chambers with very thin gas samples [25]. A better description was achieved with Monte Carlo calculations [10] but not yet with the required accuracy. Therefore, a quasi-empirical energy loss function derived for the analysis of dE/dx data from the JADE detector [7] is used in this experiment and will be described in this chapter followed by a presentation of the resulting particle separation power.

For calculating the mean energy loss, it is convenient to distinguish between soft or resonant collisions with energy transfers ($q < \eta$) where the particle interacts with the whole molecule, and hard or close collisions ($q > \eta$) where the bound electrons can be treated as quasifree particles. The intermediate energy transfer η must be large compared to the binding energy of the electrons; on the other hand, it has to be sufficiently small (η_{max}=10–100 keV) [26] so that the collision parameter is large compared to the atomic size, and the charged particle can be treated as pointlike. If the maximum measurable energy is limited by experimental conditions to values smaller than η_{max} (this is the case using the method of truncated mean) only the soft collisions contribute to the result.

The mean differential energy loss $\epsilon = \langle dE/dx \rangle$ for resonant collisions was derived by Bethe [4] as a function of the particle velocity β and charge number Q:

$$\epsilon_{q<\eta} = \xi \frac{Q^2}{\beta^2} \{ \ln(\frac{2m_e c^2 \eta}{I^2}) + \ln \beta^2\gamma^2 - \beta^2 - \delta(\beta) \} \tag{1}$$

where

$$\gamma^2 = (1-\beta^2)^{-1}$$

and

$$\xi = \nu \cdot \frac{2\pi n_e e^4}{m_e c^2} \, .$$

Here n_e denotes the electron density of the gas, m_e the electron mass, I the mean ionisation potential, $\beta = v/c$, and ν the fraction of electrons able to interact with the penetrating particle ($\nu \approx$0.9 [27]). The polarisation effect in the gas is taken into account by the density function $\delta(\beta)$ which was first introduced by Fermi [28].

Typical mean energy losses measured in this experiment are of the order of 8 keV/cm with approximately 400 electron-ion pairs created per cm of track length. Using the method of truncated mean,8a fixed fraction of all measured values is rejected. The maximum energy transfer per collision η is smaller than η_{max}=10–100 keV/cm and the energy loss formula of Bethe (eq.1) is valid.

The maximum energy transfer η is in good approximation proportional to the mean energy loss $d \cdot \epsilon(\beta, Q^2)$ in the sample of thickness d:

$$\eta = \kappa \cdot d \cdot \epsilon(\beta, Q^2)$$

The free parameter κ has to be determined from the data. With this ansatz, (1) can be rewritten as

$$\epsilon = \xi \frac{Q^2}{\beta^2} \{ K + \ln Q^2 + \ln \gamma^2 - \beta^2 - \delta(\beta) \} \tag{2}$$

where

$$K = \ln \frac{2m_e c^2}{I} + \ln \frac{\kappa d\xi}{I} + \ln \frac{\beta^2 \epsilon}{Q^2 \xi} \, .$$

Essentially the truncated mean depends on Q^2 and the particle velocity β. For increasing β the truncated mean falls with $1/\beta^2$, passes a minimum, determined by the parameter K (which is approximately constant in that region), and then rises logarithmically. The overall scale of the curve is given by the parameter ξ. When β exceeds a critical value, which depends on the density and the dielectric properties of the gas, the energy loss saturates. The function $\delta(\beta)$ contains the influence of the density and is described by a parametrisation derived by Sternheimer and Peierls [29]:

$$\begin{array}{ll} \delta = 0 & \text{for } X < X_0 \\ \delta = b \cdot (X - X_A) + a(X_1 - X)^m & \text{for } X_0 < X \leq X_1 \\ \delta = b \cdot (X - X_A) & \text{for } X_1 < X \end{array}$$

with $X = \log(\beta\gamma)$, $m = 3$, as suggested in ref. [29], and $b = 2\ln 10$.
The values for X_0 and X_1 are determined by the requirement that the energy loss function is smooth over the entire momentum range, corresponding to the boundary conditions $\delta(X_0) = 0$ and $d\delta(X_0)/dX = 0$. This yields the equations

$$X_1 - X_0 = (\tfrac{b}{ma})^{\frac{1}{m-1}} \quad \text{and} \quad X_0 = X_A - \tfrac{a(X_1 - X_0)^m}{b} \,,$$

where X_A, which determines the height of the plateau, and a are treated as free parameters. For $X > X_0$ the relativistic rise is compensated by the density function $\delta(\beta, X_A, a)$ as indicated in fig. 10, yielding a constant value (plateau) for the energy loss for $X > X_1$. The density function also absorbs the small variation of K (which is due to the term $ln\frac{\beta^2\epsilon}{Q^2\xi}$), therefore justifying the treatment of K as a constant. The values of the four free parameters (ξ,K,X_A,a) have been determined by a fit to the data and are given in table 1 together with the values obtained for JADE [7] and for the FSP of the OPAL jet chamber [13]. These measurements have been performed with slightly different gas mixtures, also given in table 1. The relativistic rise, i.e. the ratio between the plateau value and the minimum of the energy loss, was measured to be 1.466, in good agreement with previous measurements [7, 13].

	This experiment	FSP (OPAL) [13]	JADE [7]
Parameter			
ξ (keV/cm)	0.458 ± 0.001	0.5 ± 0.04	0.42 ± 0.01
K	11.91 ± 0.01	11.3 ± 1.2	13.85 ± 0.06
X_A	2.297 ± 0.004	2.1 ± 0.1	2.42 ± 0.01
a	0.251 ± 0.006	0.19 ± 0.04	0.26 ± 0.01
Gas mixture			
argon	88.2%	88.0%	88.7%
methane	9.8%	9.4%	8.5%
isobutane	2.0%	2.6%	2.8%
Relativistic rise	1.466	1.428	1.434

Table 1: Energy loss parameters obtained from different experiments, see text for details. The errors given are statistical only.

With the knowledge of the energy loss function derived above, the particle separation power D can be calculated using the measured resolution. The resolution and therefore the separation power improves with the number of useful dE/dx samples per track. The distribution of the number of useful dE/dx hits per track in multihadronic events is shown in fig. 11 for tracks with $|\cos\theta| < 0.7$. 89% of these tracks have a minimum number of hits of 40. The particle separation power in the region of the relativistic rise achieved in this way is shown in fig. 12. A separation with a probability of at least 2σ

is possible up to 13 GeV/c between electrons and pions and up to 20 GeV/c between pions and kaons or pions and protons. A separation between kaons and protons in the relativistic rise is only possible up to 1.5σ. The dependence of the separation power on the transverse momentum with respect to the jet axis has also been studied and is shown in fig. 13. The dependence is very weak and dE/dx can well be used, for example, in tagging decays of heavy quarks to electrons where the electron from the primary quark may be found in the core of the jet.

5 Summary

Already in the first year of data taking, the design goal for the resolution of the energy loss measurement in the OPAL jet chamber has been reached. All necessary corrections are well understood. The resolution allows separation of electrons and pions up to momenta of 13 GeV/c and of pions and kaons/protons up to momenta of 20 GeV/c with a probability of more than 2σ. This feature of the jet chamber has already been used in several physics analyses [30].

Acknowledgements

The successful design, construction and commissioning of the chamber would not have been possible without the outstanding efforts of all our technical collaborators in the participating institutes in Bonn, Freiburg, Heidelberg and at CERN. The contributions from our summer students P.Heimbach and C.Stegmann are well appreciated. We gratefully acknowledge the financial support of the Bundesministerium für Forschung und Technologie, FRG.

References

[1] OPAL Technical Proposal, CERN/LEPC/83-4, and
OPAL Collaboration, K.Ahmet et al., Nucl. Instr. and Meth. A305 (1991) 275.

[2] R.-D. Heuer and A. Wagner, Nucl. Instr. and Meth. A265 (1988) 11.

[3] H.M. Fischer et al., Nucl. Instr. and Meth. A283 (1989) 492.

[4] H.A.Bethe, Handbuch der Physik 24/1, J.Springer Verlag Berlin (1933) 491.

[5] I.Lehraus et al., IEEE Trans. Nucl. Sci. 30 (1983) 50.

[6] H.Drumm et al., Nucl. Instr. Meth. 176 (1980) 333, and
A.Wagner, Proc. Int. Conf. on Instrumentation for Colliding Beam Physics,
SLAC-Report 250 (1982) 76.

[7] K.Ambrus, Thesis, Univ. of Heidelberg, FRG, 1986.

[8] H.Aihara et. al, Phys. Rev. Lett. 61 (1988) 1263.

[9] A summary on experiments can be found in the Proceedings of the Int. Conf. on Instrumentation for Colliding Beam Physics, SLAC-Report 250 (1982).

[10] W.W.M.Allison and J.H.Cobb, Ann. Rev. Nucl. Part. Sci. 30 (1980) 253.

[11] W.W.M. Allison, Proc. Int. Conf. on Instrumentation for Colliding Beam Physics, SLAC-Report 250 (1982) 61.

[12] A.H.Walenta, Nucl. Instr. and Meth. 161 (1979) 45.

[13] H.Breuker et al., Nucl. Instr. and Meth. A260 (1987) 329.

[14] H.M. Fischer et al., Nucl. Instr. and Meth. A252 (1986) 331.

[15] G. Bar et al., to be submitted to Nucl. Instr. and Meth.

[16] M. Huk et al., Nucl. Instr. and Meth. A267 (1988) 107.

[17] P. v. Walter and G. Mildner, IEEE Trans. Nucl. Sci. NS-32 (1985) 626.

[18] D.Schaile et al., Nucl. Instr. and Meth. A242 (1986) 247.

[19] A. Weltin, Thesis, Univ. of Freiburg, FRG, 1987.

[20] For the potential voltage:
High voltage power supply HIGHPAC A 2K5-20HR, Oltronix Labor AG, Biel, Switzerland.
For the cathode voltages:
High voltage power supplies type HCN, from FUG Elektronik GmbH, Rosenheim, Germany.

[21] O. Biebel et al., to be submitted to Nucl. Instr. and Meth..

[22] P. Bock, private communication.

[23] H. Rieseberg, private communication.

[24] See for example D. Jeanne et al., Nucl. Instr. Meth. 111 (1973) 287.

[25] V.A. Chechin and V.C. Ermilova, Nucl. Instr. and Meth. 136 (1976) 551, and references therein.

[26] E.A. Uehling, Ann. Rev. Nucl. Sci. 4 (1954) 315.

[27] A.V. Alakoz et al., Nucl. Instr. and Meth. 124 (1975) 41.

[28] E. Fermi, Phys. Rev. Lett. 57 (1940) 485.

[29] R.M. Sternheimer and R.F. Peierls, Phys. Rev. B3 (1971) 3681.

[30] OPAL Collaboration, M.Z.Akrawy et al., Phys. Lett. B261 (1991) 334;
OPAL Collaboration, G.Alexander et al., Phys. Lett. B262 (1991) 341;
OPAL Collaboration, G.Alexander et al., CERN-PPE/91-92, subm. to Phys. Lett.

Figure Captions

Fig. 1: Expected energy loss in Ar/CH_4 at 4 bar gas pressure for different particle species as a function of momentum.

Fig. 2: Cross section through one quadrant of the OPAL jet chamber perpendicular to the beam axis and along the beam. The cathode and sense wire planes, the conical end plate (1) with the reinforcement ring at the outer radius, the shell of aluminum panels (2), barrel (3) and endcap (4) field shaping electrodes, the inner field shaping (5), the sense wire suspension (6) and the z-chambers (7) are indicated.

Fig. 3: Example of two successive hits, separated by more than 200 ns. The integrated charge of the second hit has to be corrected for the tail of the preceeding pulse (hatched area).

Fig. 4: Truncated mean (corrected for track length) as a function of the track angle θ with respect to the wire direction for 45.6 GeV/c muons from dimuon events and for (400-800) MeV/c pions in multihadronic events.

Fig. 5: Truncated mean as a function of the angle ϕ with respect to the sense wire plane for minimum ionising pions (momentum between 400 and 800 MeV/c) in multihadronic events.

Fig. 6: Truncated mean for minimum ionising pions as a function of the wire number within a sector before correction for different gains from wire to wire.

Fig. 7: Truncated mean for 45.6 GeV/c muons from dimuon events as a function of the gas density. The solid line represents a straight line fit with slope -5.1.

Fig. 8: Measured relative resolution $\frac{\sigma_{dE/dx}}{dE/dx}$ as a function of the number of samples used for the calculation of the truncated mean. Circles and crosses represent isolated tracks and tracks in multihadronic events, respectively.

Fig. 9: Truncated mean (a) for tracks in multihadronic events and dimuon events as a function of the particle momentum, (b-d) for tracks in multihadronic events in the momentum ranges 0.4–0.8, 2.5–4.0, and 6.3–10 GeV/c, respectively, and (e) for muons with momentum of 45.6 GeV/c.

Fig. 10: Calculated energy loss as function of $\beta\gamma$. The solid curve shows the result of the parametrisation as described in the text. The relativistic rise (dashed line) is compensated by the density function (dotted curve). See text for the explanation of the parameters X_0, X_A, X_1.

Fig. 11: Distribution of the number of hits per track in multihadronic events useable for the calculation of the truncated mean for tracks in the polar angle region $|\cos\theta| < 0.7$. At least 40 hits are obtained for 89% of the tracks.

Fig. 12: Particle separation power in units of $\sigma_{dE/dx}$ as a function of the particle momentum. The plot is for tracks in multihadronic events with at least 40 hits useable for the calculation of the truncated mean. The solid line indicates a separation with a probability of 2σ.

Fig. 13: Electron–pion separation in units of $\sigma_{dE/dx}$ as a function of the transverse momentum with respect to the thrust axis of the event. The curves represent different particle momenta.

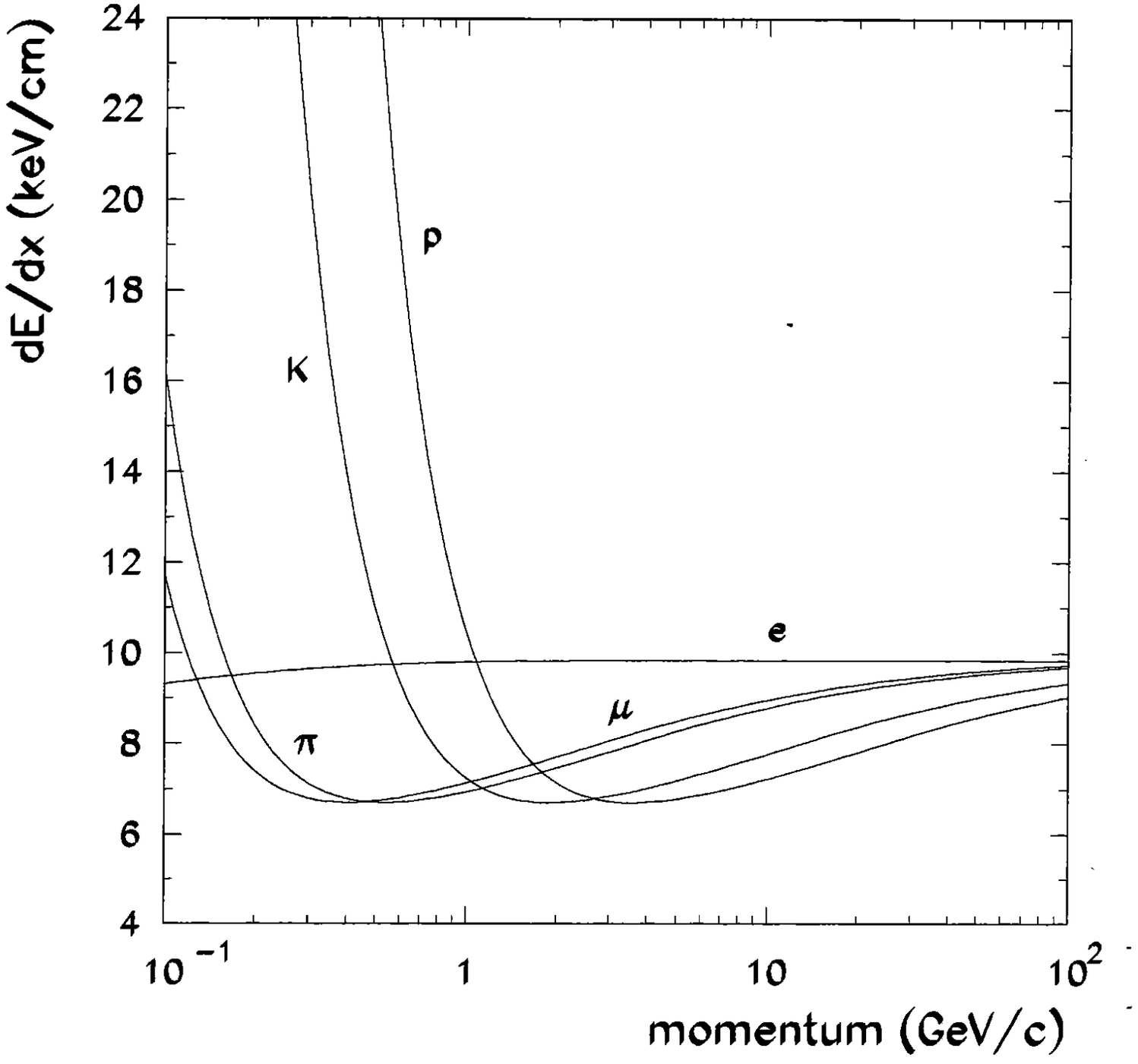
dE/dx (keV/cm)
24
22
20
18
16
14
12
10
8
6
4
p
K
e
μ
π
10 −1
1
10
10 2
momentum (GeV/c)

Fig. 1

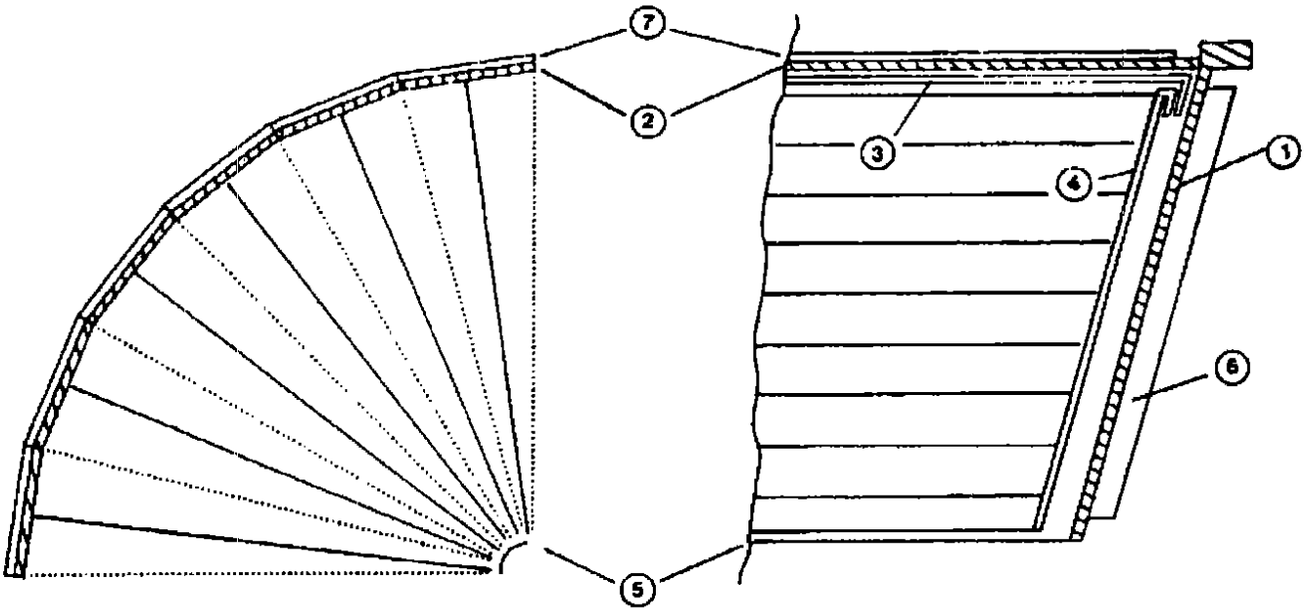

Fig. 2

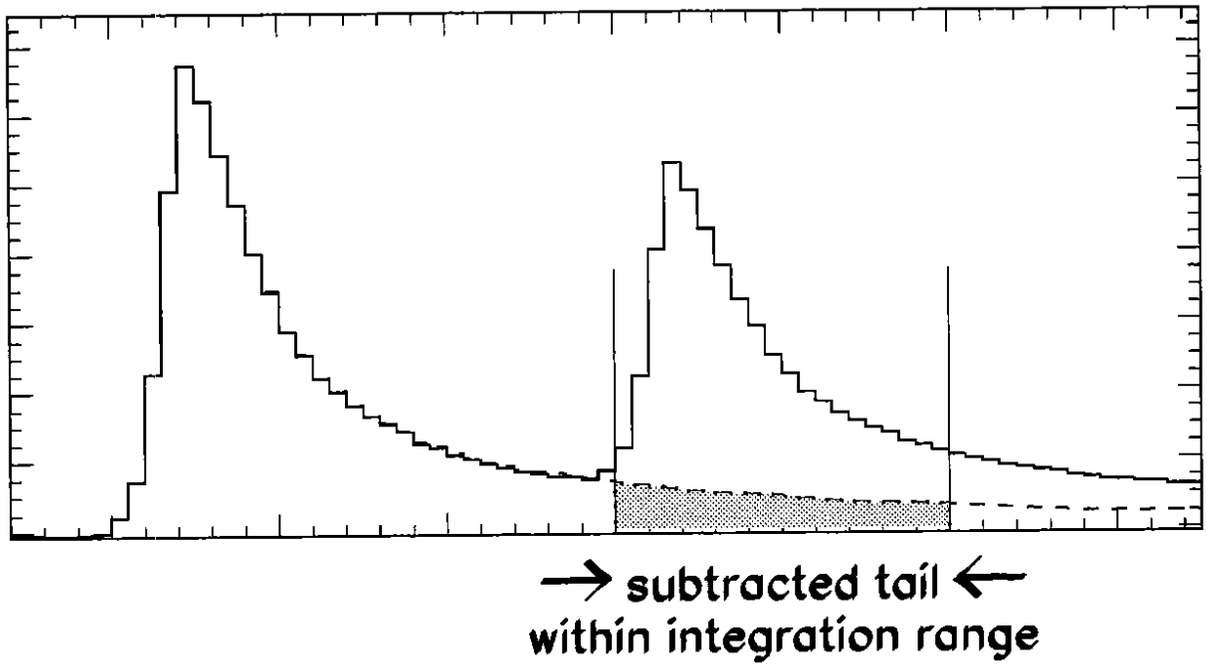

Fig. 3

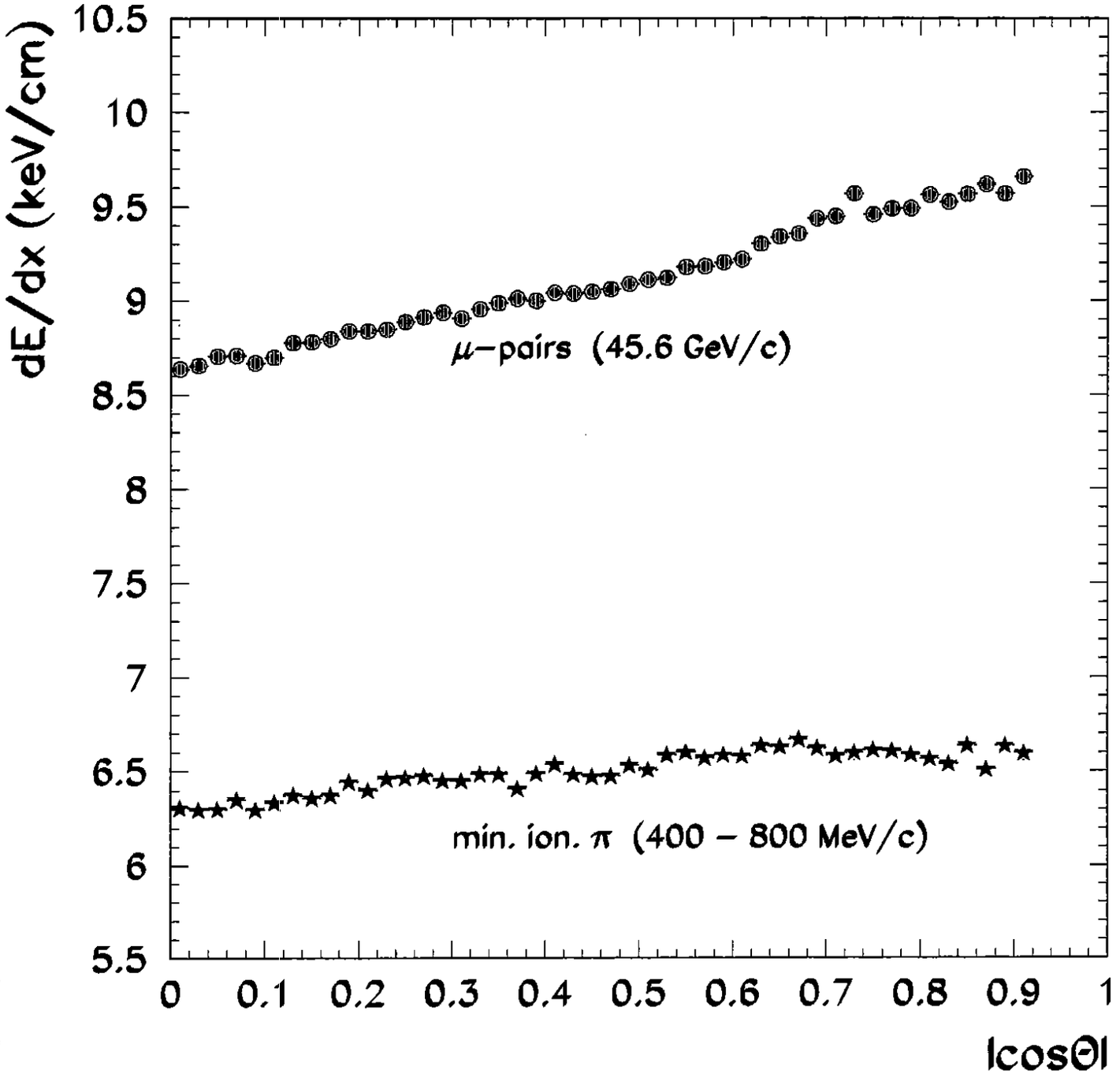
dE/dx (keV/cm)
10.5
10
9.5
9
8.5
8
7.5
7
6.5
6
5.5
0
0.1
0.2
0.3
0.4
0.5
0.6
0.7
0.8
0.9
1
|cosΘ|
μ−pairs (45.6 GeV/c)
min. ion. π (400 − 800 MeV/c)

Fig. 4

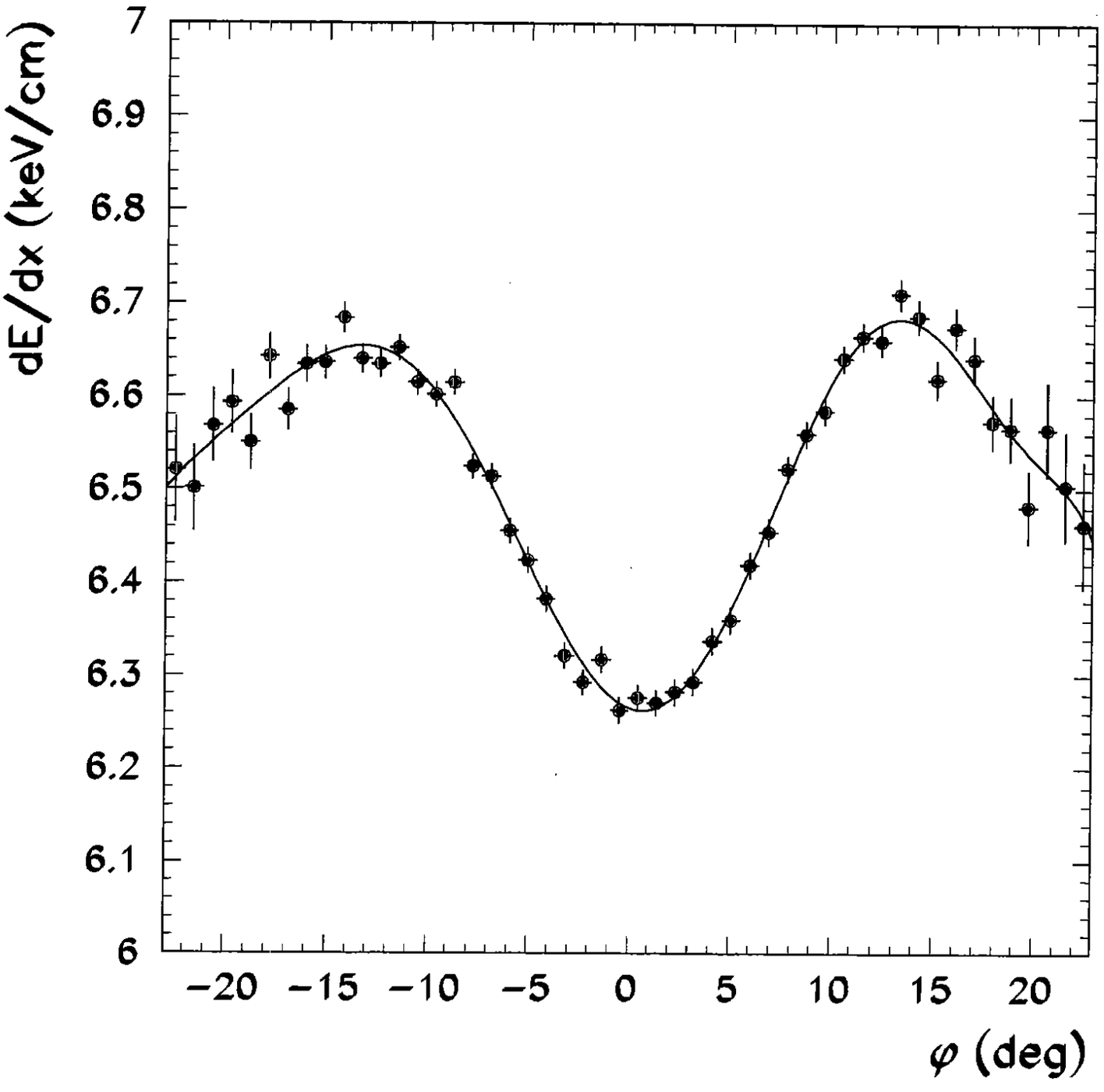

Fig. 5

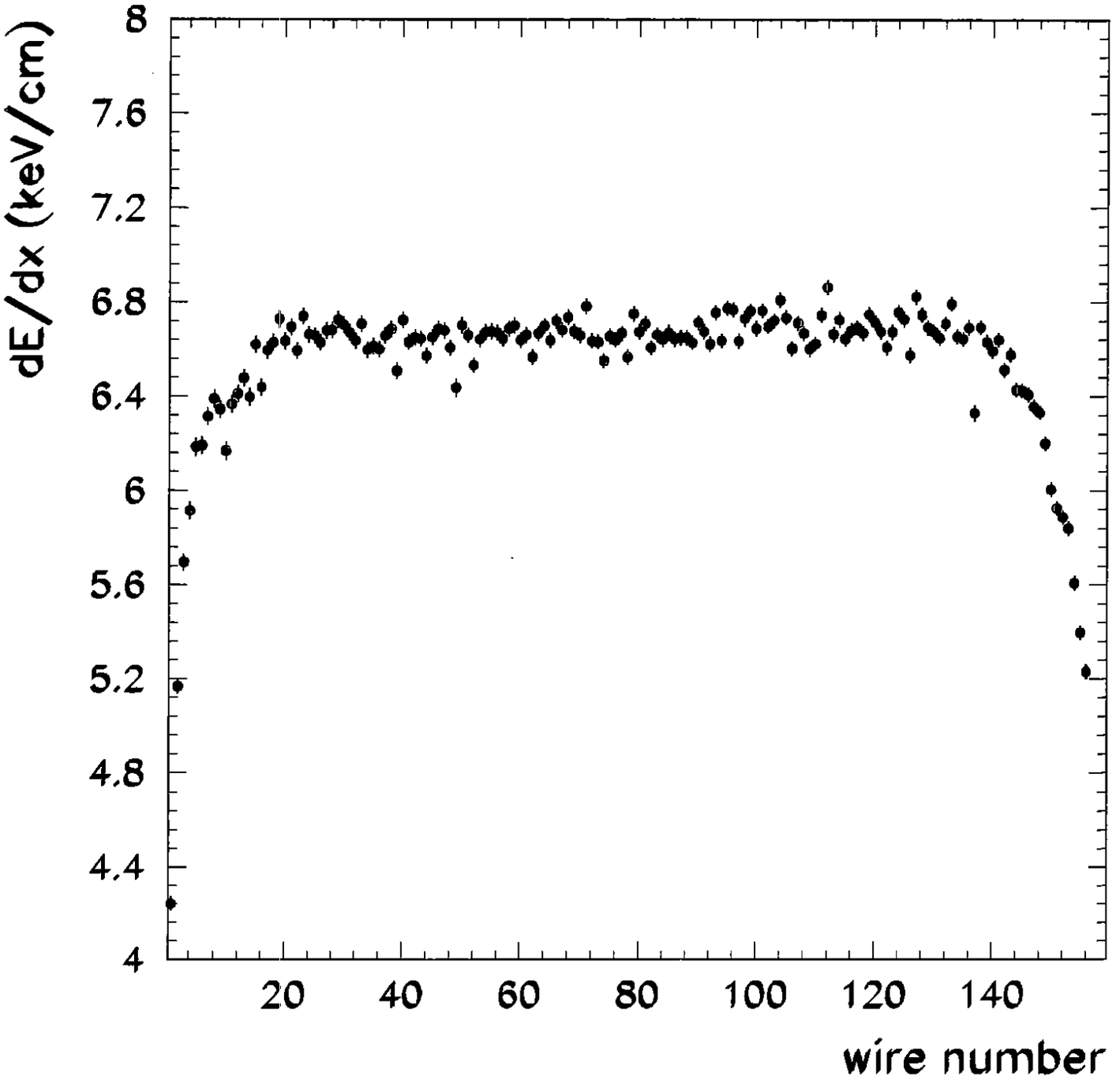
dE/dx (keV/cm)
8
7.6
7.2
6.8
6.4
6
5.6
5.2
4.8
4.4
4
20
40
60
80
100
120
140
wire number

Fig. 6

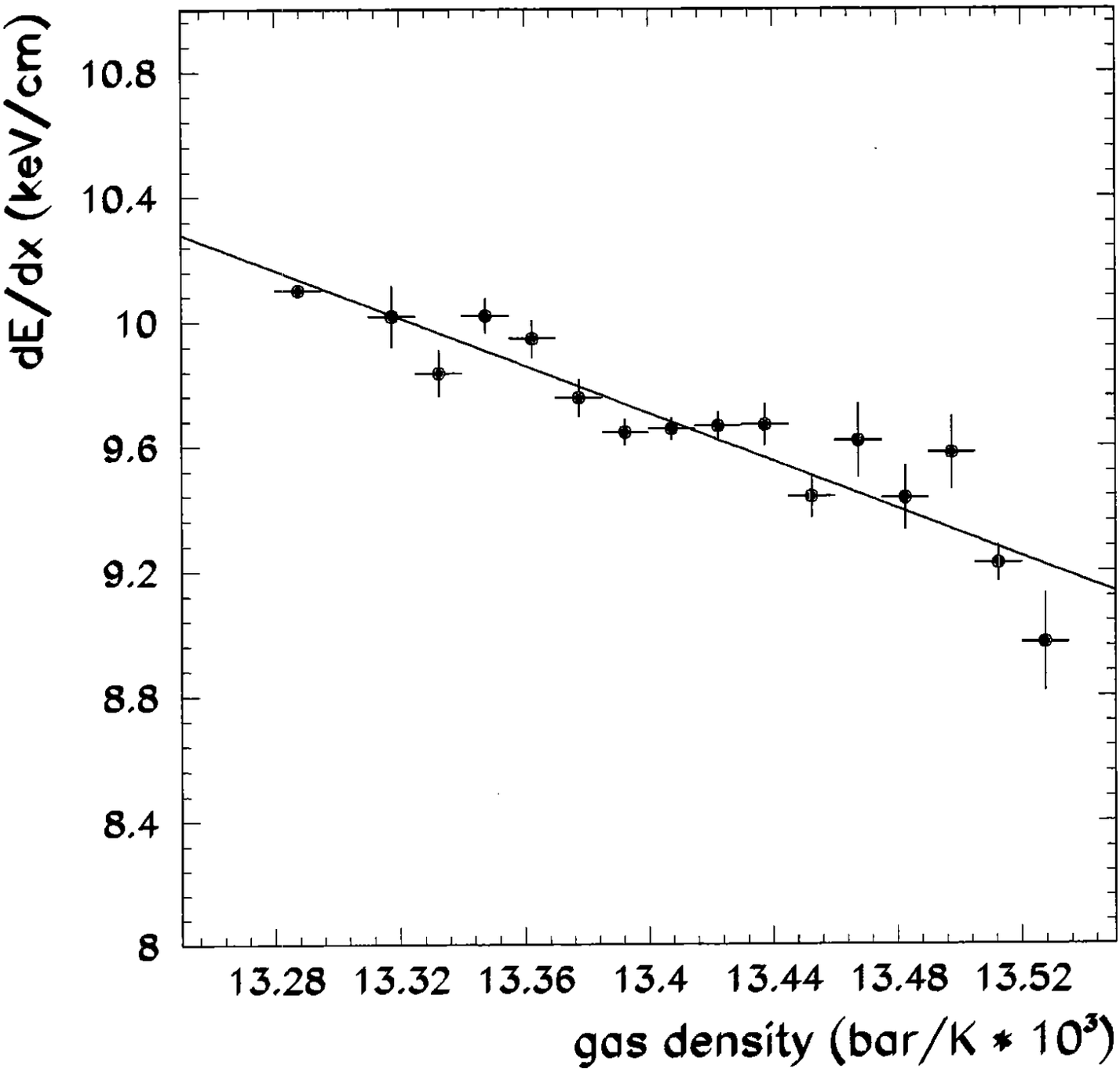
dE/dx (keV/cm)
10.8
10.4
10
9.6
9.2
8.8
8.4
8
13.28
13.32
13.36
13.4
13.44
13.48
13.52
gas density (bar/K * 10³)

Fig. 7

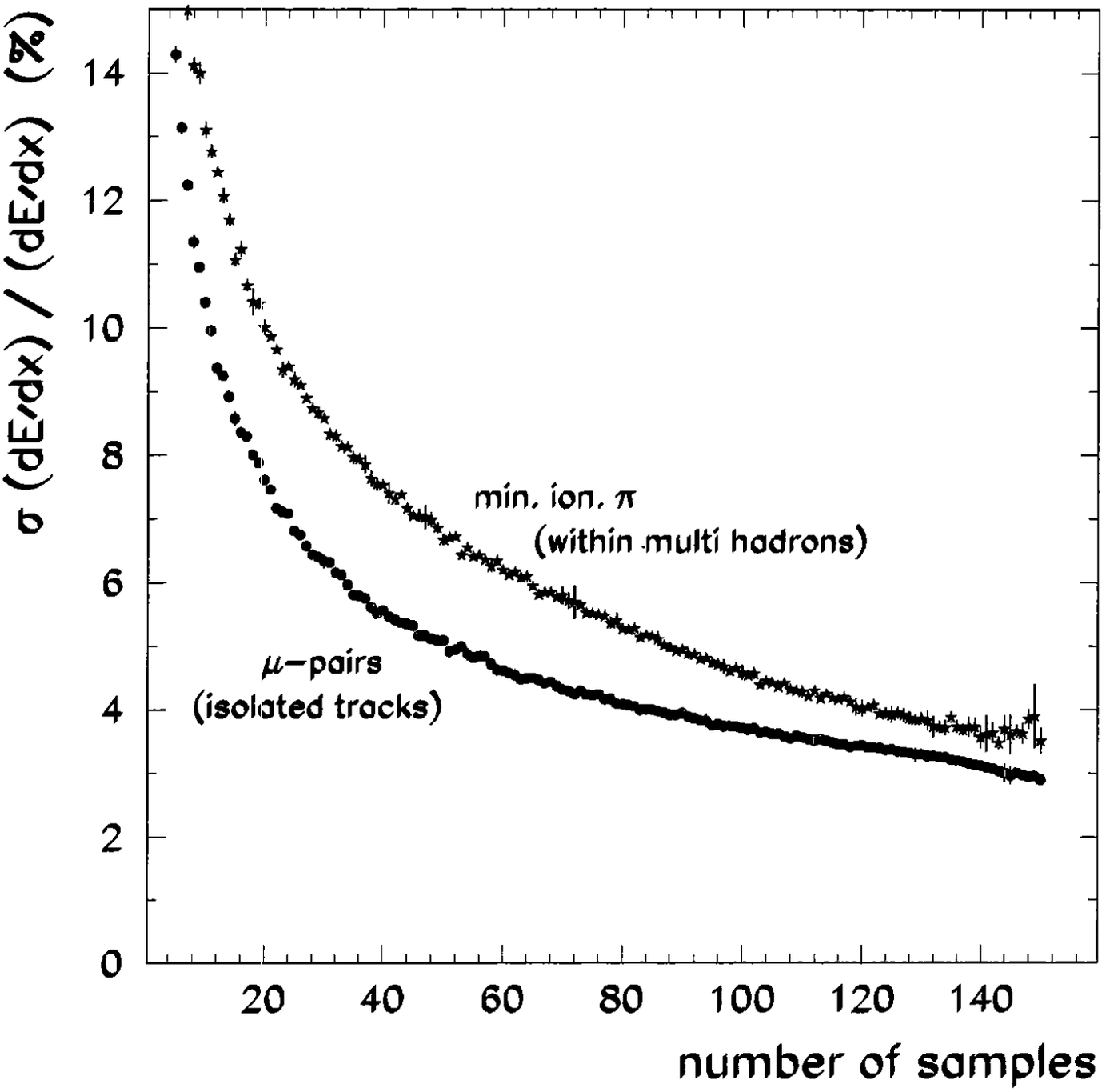
σ (dE/dx) / (dE/dx) (%)
14
12
10
8
6
4
2
0
20
40
60
80
100
120
140
number of samples
min. ion. π
(within multi hadrons)
μ−pairs
(isolated tracks)

Fig. 8

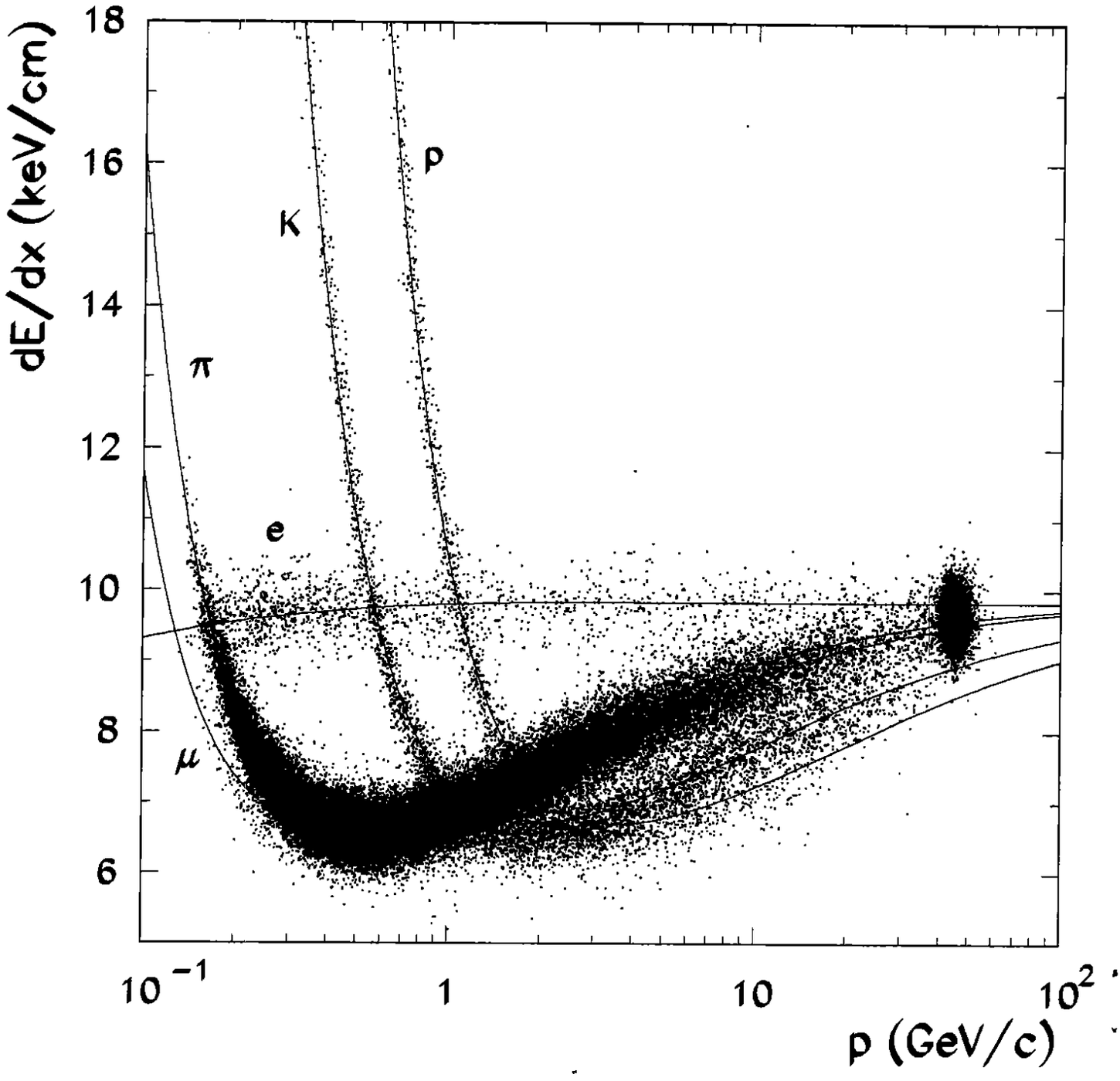

Fig. 9a

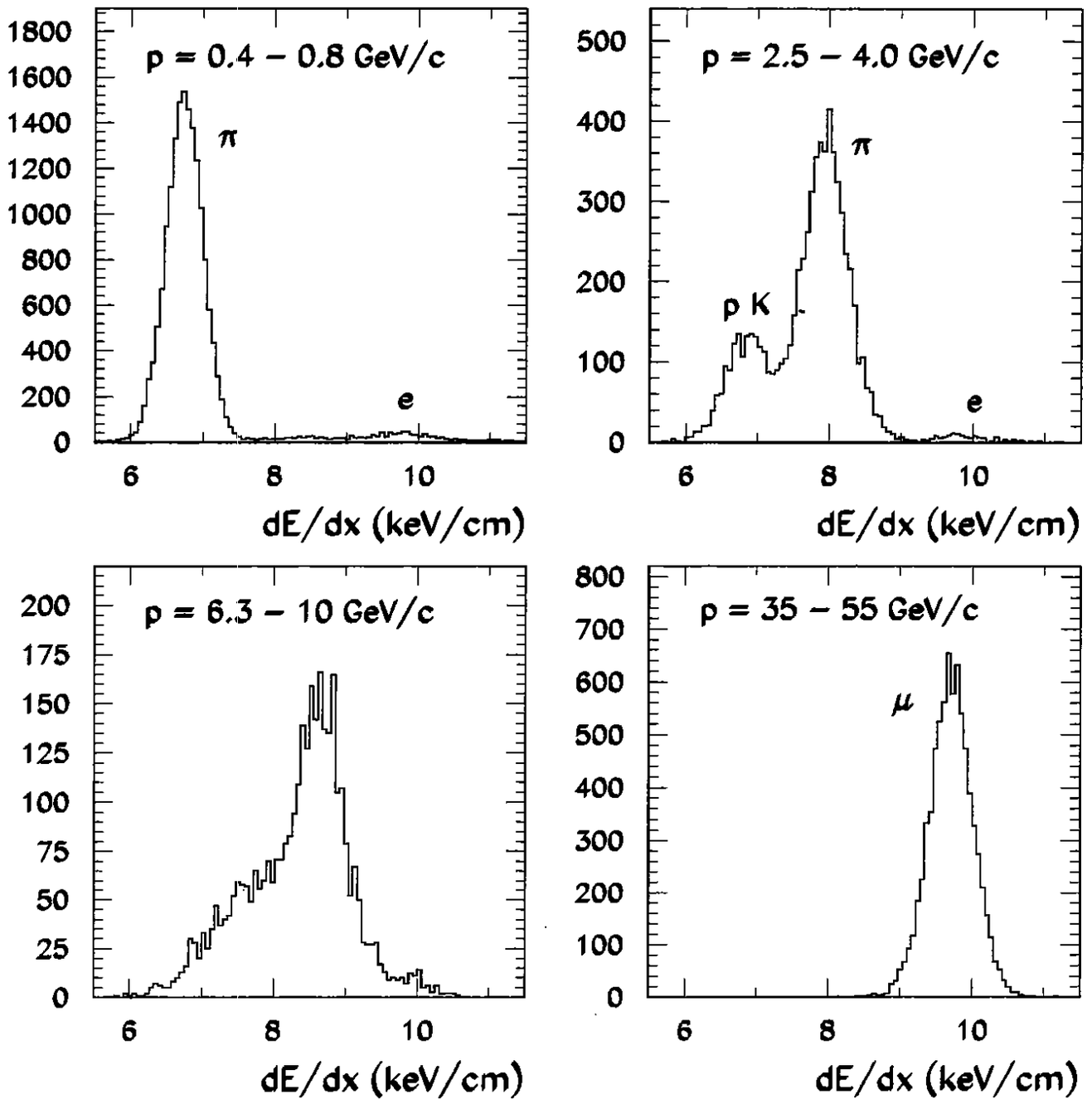
p = 0.4 – 0.8 GeV/c
π
e
dE/dx (keV/cm)
p = 2.5 – 4.0 GeV/c
π
p K
e
dE/dx (keV/cm)
p = 6.3 – 10 GeV/c
dE/dx (keV/cm)
p = 35 – 55 GeV/c
μ
dE/dx (keV/cm)

Fig. 9b-e

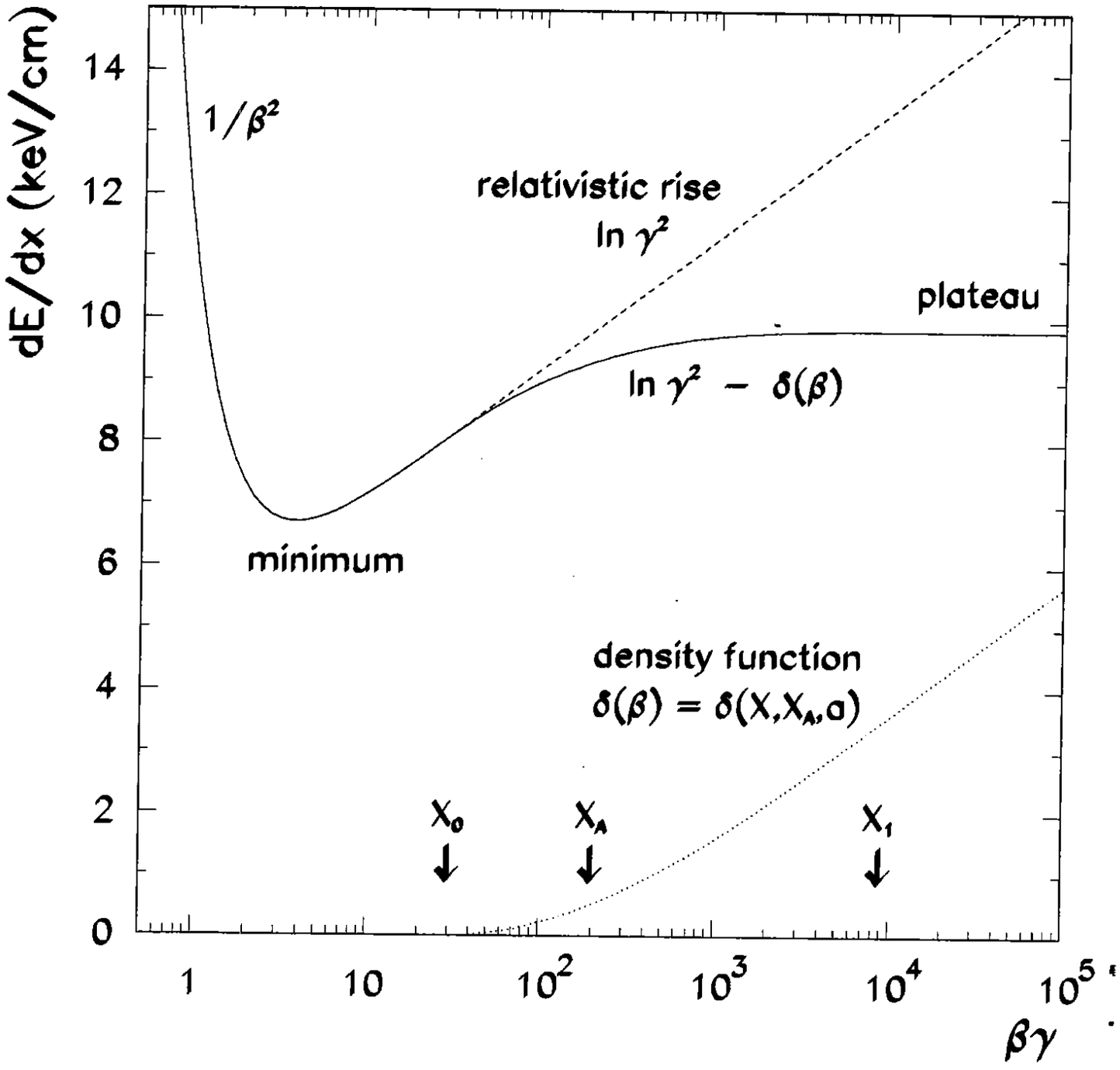
dE/dx (keV/cm)
14
12
10
8
6
4
2
0
1/β²
relativistic rise
ln γ²
plateau
ln γ² − δ(β)
minimum
density function
δ(β) = δ(X,X_A,a)
X₀
X_A
X₁
1
10
10²
10³
10⁴
10⁵
βγ

Fig. 10

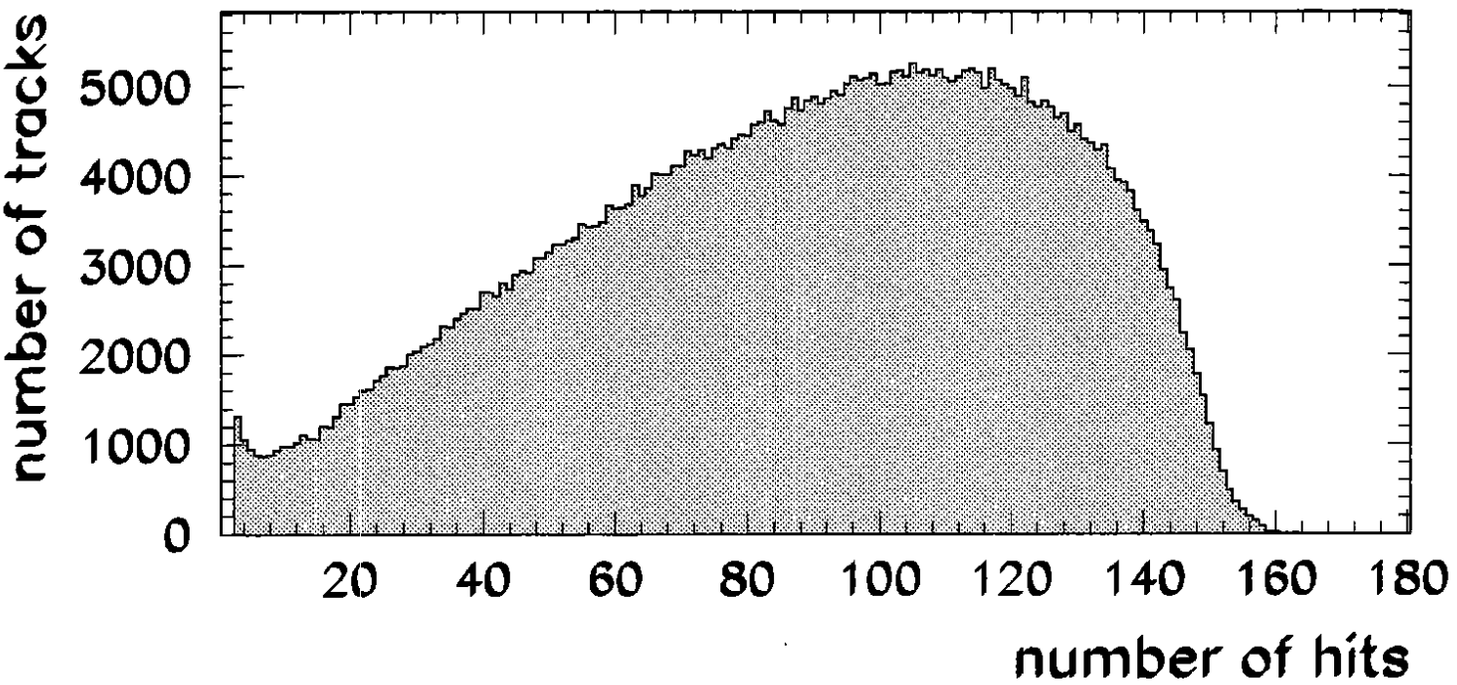
number of tracks
5000
4000
3000
2000
1000
0
20
40
60
80
100
120
140
160
180
number of hits

Fig. 11

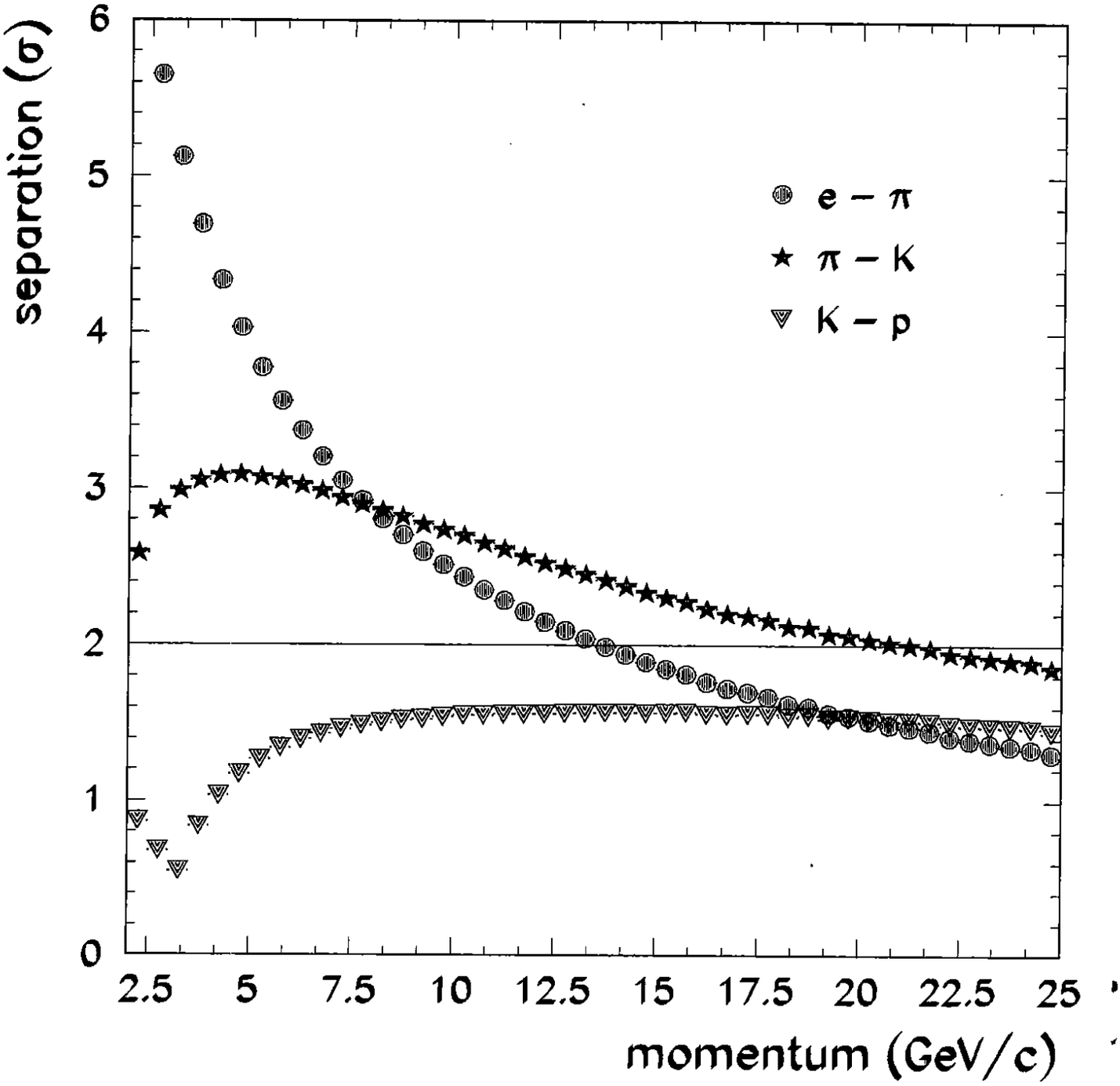
separation (σ)
momentum (GeV/c)
e − π
π − K
K − p
0
1
2
3
4
5
6
2.5
5
7.5
10
12.5
15
17.5
20
22.5
25

Fig. 12

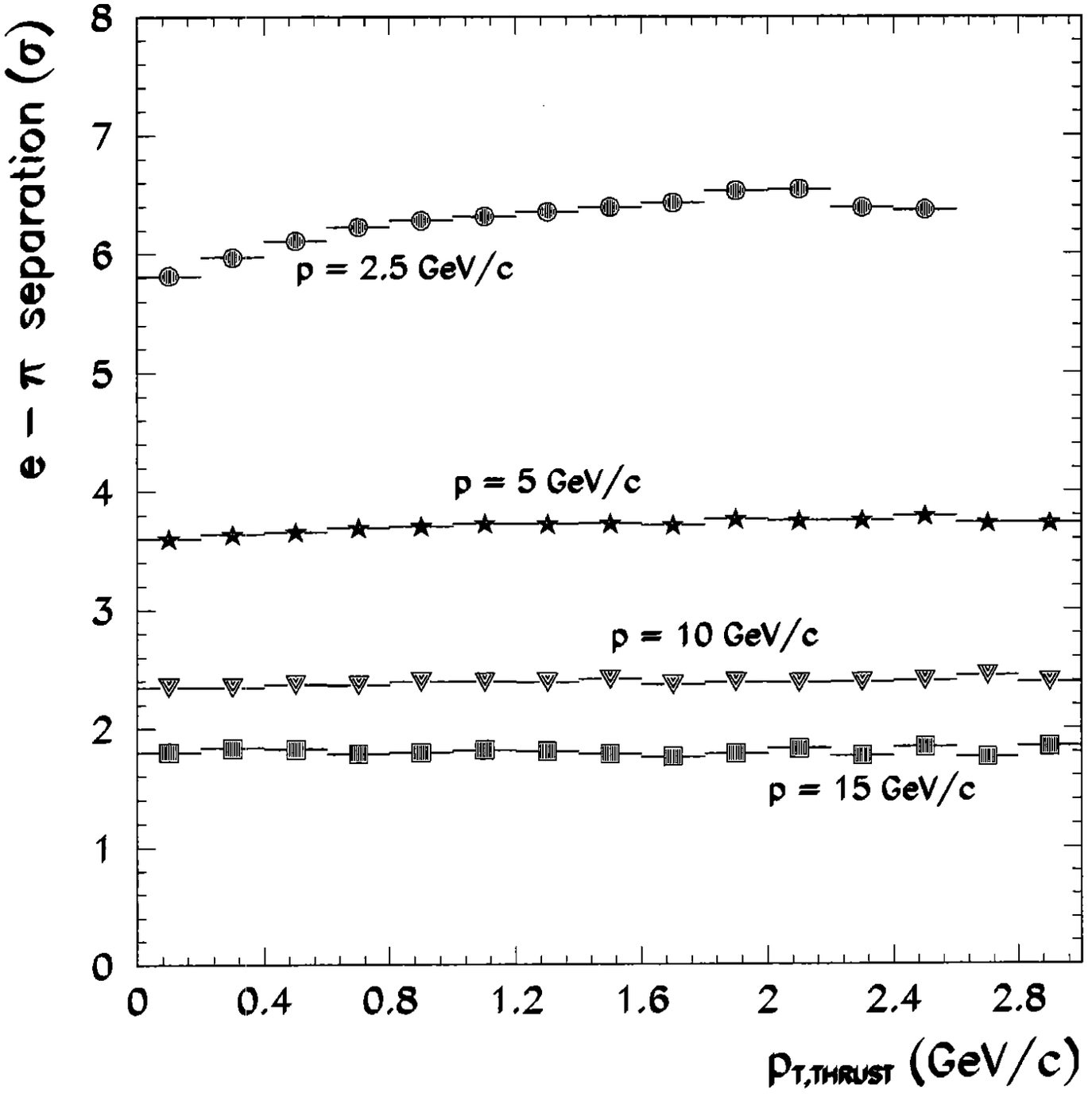
e − π separation (σ)
8
7
6
5
4
3
2
1
0
p = 2.5 GeV/c
p = 5 GeV/c
p = 10 GeV/c
p = 15 GeV/c
0
0.4
0.8
1.2
1.6
2
2.4
2.8
p_T,THRUST (GeV/c)

Fig. 13